

# Spontaneous interstitial (anti)merons in $D_{2d}$ symmetric Mn-Pt(Pd)-Sn-In system

Bimalesh Giri<sup>1</sup>, Dola Chakrabartty<sup>1</sup>, S. S. P. Parkin<sup>2</sup> and Ajaya K. Nayak<sup>1,\*</sup>

<sup>1</sup>*School of Physical Sciences, National Institute of Science Education and Research, An OCC of Homi Bhabha National Institute, Jatni-752050, India*

<sup>2</sup>*Max Planck Institute of Microstructure Physics, Weinberg 2, 06120 Halle (Saale), Germany*

\* [ajaya@niser.ac.in](mailto:ajaya@niser.ac.in)

**Interstitial topological objects, such as skyrmions, within a natural 1-D helix are predicted to be free from ambiguous 'skyrmion Hall effect'. The helical ambience precipitate an additional potential that counteract the Magnus force arising from the gyrotropic motion of skyrmion. Here, we present the observation of  $\pm \frac{1}{2}$  topological charge objects (anti)merons within the 1-D helical stripes in  $D_{2d}$  symmetric  $Mn_{1.4}Pt_{0.9}Pd_{0.1}Sn_{1-x}In_x$  system. With the help of Lorentz transmission electron microscopy study we demonstrate that the pair-wise meron and antimeron chains can be spontaneously stabilized for a critical In concentration in the system. The exchange frustration induced proportionate fragmentation of the magnetic moment in the in-plane and easy-axis directions acts as a basic ingredient for the formation of (anti)merons within the helical stripe. A constrained drift motion of (anti)merons along the stripe makes this system an ideal platform for the realization of skyrmion Hall free track motion. Moreover, the observation of (anti)merons in addition to the skyrmion and antiskyrmion in  $D_{2d}$  materials makes them a suitable horizon for zoo of topology.**

Topologically protected magnetic whirls, such as (anti)skyrmions, (anti)merons, etc., have attracted significant research interest owing to their distinctive spin textures that possess enormous possibilities in future spintronic devices. The stabilization mechanism of these complex magnetic objects relies on the underlying magnetic interactions complying with the inherent crystal symmetry of the system. For instance, antisymmetric Dzyaloshinskii–Moriya interaction (DMI) originating from the relativistic spin-orbit coupling is an essential ingredient for the stabilization of skyrmion (skx)/antiskyrmion (askx) in bulk crystals<sup>1–4</sup> and layered thin films<sup>5–8</sup> system with broken inversion symmetry. On the other hand magnetic frustration<sup>9,10</sup>, higher order exchange interaction<sup>14</sup>, dipolar interaction<sup>12,13</sup>, can stabilize skyrmions in certain centrosymmetric materials. Although independent microscopic mechanisms are responsible for the stabilization of different topological spin textures, it is interesting to study how these objects transform between two different topological states. In this direction, it has been demonstrated that application of in-plane magnetic field<sup>16,17</sup> and thermal energy modification of magnetic anisotropy<sup>18</sup> can enable overcoming the energy barrier imposed between two topological phases. Moreover, it is also proposed that the co-existence of two distinct topological objects can have significant future perspectives<sup>36</sup>. Hence, material engineering is an important pathway to achieve a delicate balance between the different energy landscapes for the realization of emergent topological magnetic phases<sup>16,21</sup>.

The topological character of skyrmions attracts a significant research interest, in particular, to study their stabilization mechanism and electrical manipulation for the application in spintronic devices<sup>5,22</sup>. However, all the topological magnetic objects with finite topological charge ( $n_{sk}$ ) show-case an unwanted 'skyrmion Hall effect', irrespective of nature of the driving field. Nonetheless,

several ideas have been proposed to mitigate the intriguing perplexity for the finite  $n_{sk}$  objects<sup>28–31</sup>. Moreover, topological objects consisting of opposite  $n_{sk}$  can intrinsically compensate the reverse gyro-tropic response, e.g. antiferromagnetic skx<sup>23–25</sup> and skyrmionium<sup>26,27</sup> are believed to be exhibit zero 'skyrmion Hall effect'. Interestingly, it has been demonstrated that the interstitial skx in a natural 1-D spin helical stripe is free from such ambiguity<sup>32–34</sup>. The confinement within the helical background accomplishes an additional potential barrier that balance the Magnus force, thereby imposing the motion along the stripe. The distinct characteristics of skx motion within helical stripes and ferromagnetic (FM) environment shift the paradigm for searching topological objects within the helical background. It has been also proposed that the meron, skyrmion, and bimerons can stabilize along with the helical stripes as natural intermediate states at the phase transition from skyrmion to helical state<sup>35</sup>. Later, Müller et al., have demonstrated the coexistence of skx with the broken helical stripe experimentally<sup>32</sup>. However, a real interstitial topological object in true helical ordered state is never observed.

The present manuscript demonstrates the first observation of natural one-dimensional helical stripes that spontaneously host a chain of merons and antimerons. In this regard, we present an extensive study on the phase stability of different topological objects in the  $D_{2d}$  symmetric system. Especially, we address the effect of exchange frustration on the ground state spin modification. To realize our goal, we consider doping of In atom in place of Sn in  $Mn_{1.4}Pt_{0.9}Pd_{0.1}Sn_{1-x}In_x$  system. It is to be noted here that the first observation of antiskyrmions has been demonstrated in  $Mn_{1.4}Pt_{0.9}Pd_{0.1}Sn$ , an inverse tetragonal Heusler system that belongs to  $D_{2d}$  crystal class<sup>4</sup>. The underlying  $D_{2d}$  crystal symmetry restricts the Dzyaloshinskii–Moriya (DM) vector within the

tetragonal basal plane with  $D_x = -D_y$ , where  $D_x$ ,  $D_y$  are DM vectors along x and y directions, respectively. Hence, the helical modulation are found only along [100] and [010] directions. Consequently, the askx lattice gets stabilized in the  $ab$  plane above the spin re-orientation temperature ( $T_{SR} \sim 130$  K)<sup>4,17,36</sup>. Powder neutron diffraction (ND) study shows the presence of a collinear and a non-collinear spin ordering above and below the  $T_{SR}$ <sup>37</sup>. Furthermore, the dipolar energy associated with the large magnetic moment of about  $\sim 5 \mu_B/\text{f.u.}$  in this system also plays a vital role in controlling the shape and size of the askx in this system<sup>38</sup>. In our previous study it has been shown that replacing Sn by In results into a non-collinear magnetic state in  $\text{Mn}_{1.5}\text{PtIn}$  with a small magnetic moment of  $\sim 1.6 \mu_B/\text{f.u.}$ <sup>39</sup>. Moreover, a comparison between the low temperature ND data of  $\text{Mn}_{1.4}\text{PtSn}$  and  $\text{Mn}_{1.5}\text{PtIn}$  sample indicates that a large magnetization can be induced in the basal plane with In doping in place of Sn. Previous theoretical study proposes that the formation of (anti)meron lattice can be energetically favorable with in-plane anisotropy<sup>40</sup>. Therefore, an effective change of the magnetization from out of plane (OP) to in-plane (IP) direction or compatible fractionation of the same in presence of the anisotropic DMI may showcase exotic topological phases like (anti)meron in the present system.

With the above discussed ideas, we present a scheme for the stability of different topological phases in the  $D_{2d}$  symmetric  $\text{Mn}_{1.4}\text{Pt}_{0.9}\text{Pd}_{0.1}\text{Sn}_{1-x}\text{In}_x$  system as shown in Fig. 1. The ground state magnetic ordering obtained from the neutron diffraction (ND) study for samples with different In concentration is presented in Fig. 1a-d. The magnetic moments of Mn atoms sitting in two different sublattices are shown by blue and red arrows. For  $x = 0.2$ , Mn moments at both the magnetic sublattices align along the c-axis, resulting in only out of plane component moment  $M_z$  above the

spin-reorientation transition  $T_{SR}$  [Fig. 1a]. In general, this type of spin arrangement favors the antiskyrmion phase as shown in Fig. 1e. Below the  $T_{SR}$ , both the magnetic sublattices exhibit a small in-plane moment  $M_x$ , however, the major component of the moment is along the c-axis, i.e.,  $M_z > M_x$  [Fig. 1b]. Formation of nontopological bubbles (NT) [Fig. 1f] is favorable in this region. For  $x \geq 0.4$ , a dominant non-collinear magnetic ordering prevails throughout the magnetic ordered phase [see Fig. 1c&d]. The Mn moments at 8d position for  $x = 0.4$  is tilted more towards the in-plane direction compared to the  $x = 0.2$  sample [see Fig. 1b & c]. Interestingly, for  $x = 0.4$  sample both the magnetization components are comparable, i.e  $M_z \sim M_x$ . The formation of (anti)meron [Fig. 1g] is expected in this sample. It is worth mentioning that for all the cases, i.e.  $x = 0.2-0.4$ , the skyrmion phase can be stabilized based on the lamellae thickness and experimental protocols. For  $x = 0.6$ , the Mn moments at the 8d position align completely in the in-plane direction. In this case,  $M_z < M_x$  and no signature of any topological phase is noticed. The variation of effective magnetic anisotropy for different  $x$  values is shown in Fig. 1h. A local minima can be visible around  $x = 0.4$ . A detailed structural and magnetic characterization along with the ND results for the present samples is presented in the Supplementary Information <sup>41</sup>.

## 1 LTEM results

For the real space visualization of the above-mentioned topological spin textures, we have carried out a detailed Lorentz transmission electron microscopy (LTEM) imaging using thin lamellae of  $Mn_{1.4}Pt_{0.9}Pd_{0.1}Sn_{1-x}In_x$  samples. Figure 2a-g depicts the over focused (OF) LTEM images recorded on the (001) oriented thin plates for  $x = 0.2$  to 0.5. The formation of triangular askx

lattice for  $x = 0.2$  at  $T = 250$  K ( $>T_{SR}$ ) can be seen from Fig. 2a. We also find the formation of hexagonal lattice of elliptical Bloch skx in this sample at  $T_{SR} < T < 250$  K<sup>41</sup>. A detailed temperature and field evolution of the skx and askx lattices is provided in the supplementary information<sup>41</sup>. Below  $T_{SR}$ , we notice that the formation of nontopological bubbles (NT) is more favorable. In fact, mixed states of skx and NT are also found in the case of thicker lamellae ( $\sim 200$  nm)[see supplementary]<sup>41</sup>. However, it is not possible to stabilize askx phase below  $T_{SR}$ . This can be understood from the fact that the dominating dipole interaction causes near degenerate energy associated with the skx, askx, and NT bubble phase in  $D_{2d}$  symmetric materials. As it can be seen from Fig. 2b, the skx and askx phases coexists in case of  $x = 0.3$ . The weak energy barrier among them can be overcome and envisaged through the application of an in-plane magnetic field, hence, a reversible transformation between skx, NT, and askx can be realized<sup>17</sup>. In case of  $x = 0.4$ , the appearance of triangular lattice of the NT bubbles at  $T > T_{SR}$  and the conjunction of NT bubbles and skx at  $T < T_{SR}$  is shown in Fig. 2c & d, respectively. In the present system, topologically trivial and non-trivial magnetic textures are present for In concentration up to  $x = 0.4$ . For  $x = 0.5$ , we do not find any magnetic contrast ( Fig. 2e).

**Spontaneous (anti)merons:** Now, we concentrate on the  $x = 0.4$  sample that exhibits a non-collinear magnetic ordering throughout the ordered phase and satisfies the criteria of  $M_z \sim M_x$ . At zero magnetic field this sample shows the usual helical phase, consistent with the  $D_{2d}$  symmetric system. Interestingly, at temperature  $T = 112$  K, nanometric size local dark and bright dots start appearing in the interstitial position of the helical stripes [Fig. 2f]. With further lowering the temperature to  $T = 100$  K (the lowest possible temperature achievable in our system), the

magnetic contrast of these dots become very prominent as can be seen in Fig. 2g. In addition, these interstitial dots appear with alternate black and white chain without any periodicity, as the distance between two pair of chains is not equal (Fig. 2g). These dark and bright dots may refer to the formation of nanometric size swirling spin textures. To confirm the nature of these interstitial spin textures, we have performed transport of intensity equation (TIE) mapping of the LTEM images taken in in-focus, under-focus and over-focus conditions. Figure 2h&i show the in-plane magnetization mapping and spin curling of the selected dots marked in the blue and violet dashed rectangles in Fig. 2g. The nature of the local magnetic field variation clearly establish that these interstitial objects are meron and antimerons. The (anti)merons are vortex-like topological objects with a core up/down and in-plane peripheral spin distribution that carry a topological charge  $n_{Sk} = \pm \frac{1}{2}$ . They are different from half (anti)skyrmions which also hold  $n_{Sk} = \pm \frac{1}{2}$  and are found at the edge of the thin lamellae of  $\text{Mn}_{1.4}\text{Pt}_{0.9}\text{Pd}_{0.1}\text{Sn}$ <sup>42</sup>. Although it is difficult to determine the exact core spin direction of the(anti)merons from the LTEM contrast, it can be safely said that if the meron is with upward core, the antimeron must be a downward core spin as the z-component of the moment is maximum/minimum (upward/downward) at the middle of the dark and bright helical stripe. Therefore, the bright spots are meron with downward core spins, and the black spots are antimerons with upward core spins. We reach this conjecture by analogy with the LTEM contrast of the simulated spin texture, which will be discuss later.

**Field evolution of (anti)merons and their motion** In the present system the (anti)merons appear spontaneously by cooling the sample from the paramagnetic state. Therefore, it is important to understand their stability under the external magnetic field. Figure 3a-e depicts the field evolution

of the pair of meron and antimeron chains. The interstitial (anti)merons are stable up to a field of 0.07 T [see Fig. 3a-d]. For higher fields (anti)merons disappear, resulting in only the helical stripe phase [see Fig. 3e]. We observe that the (anti)meron chains are not reversible under field reversal. Interestingly, the (anti)merons chains start drifting with the application of external magnetic field. It can be seen that the (anti)meron chain with bright contrast remains almost fixed in its position, whereas a gradual shift of the meron chain with dark spots is visible. Figure 3f describes the field-dependent separation length of the pair of (anti)merons chains. Importantly, the drift is constrained along the stripe only. All the images were taken close to the pole positions so that the effect of the in-plane field is negligible in their drift motion. This study clearly demonstrates the motion of (anti)merons along the stripes.

## 2 Micromagnetic Simulation

All our experimental results show that the present  $\text{Mn}_{1.4}\text{Pt}_{0.9}\text{Pd}_{0.1}\text{Sn}_{1-x}\text{In}_x$  samples with  $x = 0$  to 0.4, can host different topological magnetic states depending on the temperature and magnetic field application. The stability of skyrmions in  $D_{2d}$  symmetric materials is well described by the Hamiltonian written as-

$$\begin{aligned}
H = & -J \sum_i m_i \cdot (m_{i+\hat{a}} + m_{i+\hat{b}} + m_{i+\hat{c}}) \\
& +D \sum_i (m_i \times m_{i+\hat{a}} \cdot \hat{a} + m_i \times m_{i+\hat{b}} \cdot \hat{b}) \\
& +K \sum_i (m_{c,i})^2 - H \sum_i m_{c,i},
\end{aligned} \tag{1}$$

where the first and second terms are the conventional isotropic exchange and Dzyaloshinskii-Moriya interaction; the third and fourth terms are the uniaxial anisotropy and Zeeman energy,

respectively.  $\hat{a}$ ,  $\hat{b}$ ,  $\hat{c}$  are the unit vectors in the Cartesian co-ordinate system. It is well understood that the competition between anisotropic DMI and isotropic exchange interaction governs the propagation of helical state along [100] and [010] directions. The application of the magnetic field along the anisotropic magnetic axis converts the helical state into skyrmion lattices. The large magnetization in these materials causes dominant dipolar interaction depending on the lamellae thickness and temperature<sup>38</sup>. Moreover, the dipolar energy can overtake the anisotropic DMI and compete with the anisotropy to stabilize elliptical skyrmion at lower temperature region<sup>17,36</sup>. The elongation direction of these elliptical objects remains to constrain along [100] and [010] only. Theoretically, the skyrmion lattice can be stabilized in an easy-plane magnetic system under an external field and can be transformed into the (anti)meron lattice state by increasing the easy-plane anisotropy<sup>40</sup>. Most of the system show the (anti)merons as a lattice<sup>16</sup>, inside a domain wall<sup>15,18</sup>, and as isolated one in an easy plane magnetic system<sup>44,45</sup>.

In the present In doped samples, the magnetic moment partially aligns in the plane direction with a large magnetization component in the basal plane [see Fig. 1b-d]. To understand the origin of the (anti)merons formation in the present system, we have carried out a detailed micromagnetic simulations by implementing easy-plane anisotropy. We set up  $H = 0$  to echo the experimental observation. Therefore, the effective Hamiltonian contains ferromagnetic exchange, anisotropic DMI, and easy-plane anisotropy. We take random magnetization as an initial state and relax the system to stabilize the (anti)meron pairs formed only after cooling the system to a low temperature from a paramagnetic state [see Fig. 2f & g]. Figure 4a-c shows the magnetization configuration for different values of in-plane anisotropy constant ( $K_u$ ). For low values of  $K_u$ , some paired and

isolated anitskyrmions are formed [see Fig. 4a]. Further increasing the in-plane anisotropy in the presence of DMI mainly results in a non-collinear in-plane magnetic state. For  $K_u = 2.0 \times 10^5$  J/m<sup>3</sup>, local meron-antimeron chains are stabilized within the non-collinear spin configurations [Fig. 4b]. We find the formation of both core up and down merons and antimerons as marked in red and blue color circles in Fig. 4b. By further increasing the  $K_u$ , mostly collinear in-plane magnetic state gets stabilized with some isolated chains and single (anti)meron [Fig. 4c]. The simulated results in Fig. 4b closely corroborate our experimental finding of spontaneous (anti)merons in the system. For a better correspondence of the experimental results with the simulated one, the LTEM contrast of the magnetization configuration in Fig. 4b is shown in Fig. 4d. The LTEM contrast is sensitive only to the twisting of the spins, e.g. the domain wall, vortices, etc. The bright spots appearing within the fainted bright stripes in Fig. 4d corresponds to the core down Bloch-type meron [shown within blue circle in Fig. 4e]. Similarly, core up merons appear as dark spots within the fainted dark stripes [shown in red circle of Fig. 4e]. These simulated spin textures fully corroborate our experimental results. To justify the particle-like nature of these local objects, we calculate the topological charge density (TCD)<sup>53</sup>, as shown in Fig. 4f. The TCD of these localized objects follows the definition given as  $n_{sk} = \frac{pw}{2}$ , where,  $p$  = polarization of the core spin (+1 for up, -1 for down) and  $w$  is the winding number ( $w = +1$  for vortex,  $w = -1$  for antivortex)<sup>43</sup>. Therefore, a meron-antimeron pair with opposite core spin polarity can lead to a total topological charge of +1 or -1.

### 3 Discussions and Conclusion

In the earlier studies, Gao et al. have shown that a delicate fractionation of the magnetization results in the spontaneous formation of domain wall (anti)merons in the ferromagnetic in  $\text{Fe}_{5-x}\text{GeTe}_2$  <sup>15</sup>. Similarly, in the amorphous easy-plane ferrimagnetic Gd-Fe-Co system, the periodic appearance of Bloch lines within the Bloch domain wall is responsible for the formation of meron-antimeron chains <sup>18</sup>. In case of  $\beta$ -Mn type  $\text{Co}_8\text{Zn}_9\text{Mn}_3$ , the origin of square lattice (anti)merons is assigned to the overlapping between two orthogonal helices propagating in the plane perpendicular to the magnetic field <sup>16</sup>. Nonetheless, several theoretical studies have indicated the variation in magnetic anisotropy can lead to the emergence of a topological (anti)merons <sup>40,46</sup>.

In the present case the doping of In in place of Sn serves two purposes. First, since the magnetic Mn concentration does not change, the effect of magnetic disorder in the system can be avoided. Secondly, the addition or reduction in the valence electron count maximally impacts the magnetic interactions, which is linked to the higher power of moments, such as Ruderman-Kittel-Kasuya-Yosida (RKKY), biquadratic ( $\propto (S_i \cdot S_j)^2$ )<sup>47</sup>, and topological-chiral interaction ( $\propto [S_i \cdot (S_j \times S_k)]^2$ )<sup>48</sup>. In a metallic system, the effective exchange strength may not be limited to the nearest neighbor site only. The itinerant electron can give rise to an oscillatory RKKY-type interaction which is extended beyond the nearest neighbor. For instance, a spin-canted state arises in  $\text{Mn}_2\text{Y}(=\text{Rh}, \text{Pt}, \text{Ir})\text{Z}$  due to the exchange frustration mediated through RKKY interaction <sup>49</sup>. Swekis et al. have shown that the origin of the spin re-orientation transition in  $\text{Mn}_{1.5}\text{PtSn}$  can be associated with the exchange frustration in the system <sup>50</sup>. Hence, the presence of spin-canted state

in the present system can be connected to the exchange frustrations arising due to addition of extra electron to the system. As a result, the net canted magnetic moment in the OP/IP direction systematically decreases/increases with In concentration. Therefore, in the present system a gradual shift in the major magnetic component is attributed to the re-alignment of the magnetic anisotropy. The proportionate IP and OP moment in presence of anisotropic DMI in the  $D_{2d}$  symmetric system can result in interstitial (anti)meron chains. This is also supported by our micromagnetic simulations.

In summary, we present a comprehensive study on the finding of different topological magnetic phases in the  $D_{2d}$  symmetric tetragonal Heusler system  $\text{Mn}_{1.4}\text{Pt}_{0.9}\text{Pd}_{0.1}\text{Sn}_{1-x}\text{In}_x$ . The stabilization of these topological objects are well connected with the systematic change in the magnetic structure with different degrees of non-collinearity arising due to exchange frustration in the system. The antiskyrmion phase stabilizes only when the underlying spins are collinear in nature, whereas the non-topological bubbles are more favorable in the noncollinear background spin. At a critical noncollinear magnetic state where  $M_z \sim M_x$ , we find the simultaneous presence of helical stripes and (anti)meron chains. Most importantly, the drift motion of the (anti)meron chains along the helical stripe under an external magnetic field mimics the 1-D-like deflection-free movement. Therefore, our proposition of interstitial (anti)merons with  $\pm \frac{1}{2}$  topological charge can be a potential alternative for the future development of 'race track memory'.

## Methods

**Experimental methods** Polycrystalline samples of  $\text{Mn}_{1.4}\text{Pt}_{0.9}\text{Pd}_{0.1}\text{Sn}_{1-x}\text{In}_x$  were prepared by arc

melting the stoichiometric amount of high-purity constituent elements. The samples were kept at 750°C for seven days after being sealed in high vacuum quartz tubes. The structural phase of the samples was confirmed by room temperature powder X-ray diffraction (XRD) using Cu-K $\alpha$  radiation (Rigaku). The composition and homogeneity of the samples were checked in field emission scanning electron microscopy (FESEM) and energy dispersive X-ray spectroscopy (EDS). Magnetic measurements were carried out using superconducting quantum interference device vibrating sample magnetometer (SQUID VSM) (MPMS-3). Electron back scattered diffraction (EBSD) was used to find the suitable grain for lamellae preparation from the polycrystalline samples. The transmission electron microscopy (TEM) lamellae were prepared using a 30 kV Ga ion-based Focused Ion Beam (FIB). A very low dose factor was used to thin down the lamellae to desired thickness. The (001) orientation of the lamella was confirmed by performing the selected area electron diffraction (SAED) in 200 kV JEOL TEM (JEM-F200). The magnetic contrast was observed using the Lorentz TEM (LTEM) mode. A double-tilting liquid nitrogen-based sample holder (GATAN-636) was used for temperature dependent LTEM imaging.

**Transport of intensity equation (TIE)** LTEM imaging is a versatile technique to visualize various nano- to micro-scale magnetic textures in thin lamella samples. Interaction of the electron with the in-plane magnetic field of the sample results in the convergence(divergence) of the electron beam that produces bright(dark) contrast under different defocus conditions. If a magnetic image appears as bright in over focus (OF) condition, then it should be dark in the under focus (UF) and vice versa. Extraction of the actual spin texture is possible by solving the transport of intensity equation (TIE) from the intensity map of the series of digital images. The TIE solves the

differential equation between intensity and electrons phase have given as-

$$\frac{2\pi}{\lambda} \frac{\partial^2 I(x, y, z)}{\partial^2 z} = -\nabla_{xy} \cdot [I(x, y, z) \nabla_{xy} \phi(x, y, z)], \quad (2)$$

where,  $\lambda$  is electron wavelength,  $I$  is intensity of the electrons beam, and  $\phi$  is the phase of electrons.

A series of systematic images can be acquired to map the in-plane magnetization distribution of the thin lamella. For example, an equal defocus length of UF and OF, along with an in-focus (IF) image, can be used to map out the magnetization distribution. First, we extracted the electron-phase images and then mapped out the magnetization textures using the software QPt<sup>54</sup>.

**Micromagnetic simulation** Micromagnetic simulations are carried out using Object Oriented Micro Magnetic Framework OOMMF<sup>51</sup> to understand the possible mechanism of (anti)meron formation in  $D_{2d}$  symmetric materials. We have taken a slab dimension of  $250 \times 250 \times 10 \text{ nm}^3$  and the unit cell dimension of  $1 \times 1 \times 1 \text{ nm}^3$ . The Gilbert damping parameter ( $\alpha$ ) was set at 0.5. We have fixed the exchange strength ( $J$ ) = 1.2 pJ/m, and DMI strength ( $D$ ) = 0.5 mJ/m<sup>2</sup>, saturation magnetisation ( $M_s$ ) =  $7 \times 10^5 \text{ A/m}$ , and applied magnetic field ( $H$ ) = 0. The in-plane anisotropy ( $K_u$ ) was varied in the range of  $1.0$ - $3.0 \times 10^5 \text{ J/m}^3$  to stabilize a meron-antimeron chain within the helical-like stripes.

### **Data availability**

All data used to obtain the conclusions in this paper are presented in the paper and/or the Supplementary Materials. Other data may be requested from the authors. Please direct all inquiries to A.K.N. (ajaya@niser.ac.in).

## References

1. Mühlbauer, S. et al. Skyrmion lattice in a chiral magnet. *Science* **323**, 915 (2009).
2. Yu, X. Z. et al. Real-space observation of a two-dimensional skyrmion crystal. *Nature (London)* **465**, 901 (2010).
3. Adams, T. et al. Long-Wavelength helimagnetic order and skyrmion lattice phase in  $\text{Cu}_2\text{OSeO}_3$ . *Phys. Rev. Lett.* **108**, 237204, 2012.
4. Nayak, A. K. et al. Magnetic antiskyrmions above room temperature in tetragonal Heusler materials. *Nature (London)* **548**, 561 (2017).
5. Sampaio, J. et al., Nucleation, stability and current-induced motion of isolated magnetic skyrmions in nanostructures. *Nat. Nanotechnol.* **8**, 839–844 (2013).
6. Jiang, W. et al. Blowing magnetic skyrmion bubbles. *Science* **349**, 283–286, (2015).
7. Moreau-Luchaire, C. et al. Additive interfacial chiral interaction in multilayers for stabilization of small individual skyrmions at room temperature *Nat. Nanotechnol.* **11**, 444–448 (2018).
8. Soumyanarayanan, A. et al. Tunable room-temperature magnetic skyrmions in Ir/Fe/Co/Pt multilayers. *Nat. Mater* **16**, 898–904 (2017).
9. Okubo, T. Chung, S. & Kawamura, H. Multiple- $q$  States and the Skyrmion Lattice of the Triangular-Lattice Heisenberg Antiferromagnet under Magnetic Fields. *Phys. Rev. Lett.* **108**, 017206 (2012).

10. Leonov A. O. & Mostovoy, M. Multiply periodic states and isolated skyrmions in an anisotropic frustrated magnet. *Nat. Commun.* **6**, 8275 (2015).
11. Zhang, X. et al. Skyrmion dynamics in a frustrated ferromagnetic film and current-induced helicity locking-unlocking transition. *Nat. Commun.* **8**, 1717 (2017).
12. Yu, X. et al. Magnetic stripes and skyrmions with helicity reversals. *Proc. Natl Acad. Sci.* **109**, 8856–8860 (2012).
13. Chakrabartty, D. et al., Tunable room temperature magnetic skyrmions in centrosymmetric kagome magnet  $\text{Mn}_4\text{Ga}_2\text{Sn}$ . *Communications Physics* **5**, 189 (2022).
14. Heinze, S. et al. Spontaneous atomic-scale magnetic skyrmion lattice in two dimensions. *Nat. Phys.* **7**, 713–718 (2011).
15. Gao, Y. et al. Spontaneous (Anti)meron Chains in the Domain Walls of van der Waals Ferromagnetic  $\text{Fe}_{5-x}\text{GeTe}_2$ . *Adv. Mater.* **32**, 2005228, 2020.
16. Yu, X. Z. et al. Transformation between meron and skyrmion topological spin textures in a chiral magnet. *Nature* **564**, 95-98, 2018.
17. Peng, L. Controlled transformation of skyrmions and antiskyrmions in a non-centrosymmetric magnet. *Nat. Nanotechnol.* **15**, 181–186 (2020).
18. Li, Z. et al., Field-free topological behavior in the magnetic domain wall of ferrimagnetic  $\text{GdFeCo}$ . *Nat. Commun.* **12**, 5604 (2021).

19. Vir, P. et al. Anisotropic topological Hall effect with real and momentum space Berry curvature in the antiskyrmion-hosting Heusler compound  $\text{Mn}_{1.4}\text{PtSn}$ . *Phys. Rev. B* **99**, 140406(R) (2019).
20. Jena, J. Evolution and competition between chiral spin textures in nanostripes with  $D_{2d}$  symmetry. *Sci. Adv.* **6** (49), eabc0723 (2020).
21. Karube, K. et al. Disordered skyrmion phase stabilized by magnetic frustration in a chiral magnet. *Sci. Adv.*, **4** (9), eaar7043 (2018).
22. Huang, S. et al. Stabilization and current-induced motion of antiskyrmion in the presence of anisotropic Dzyaloshinskii-Moriya interaction. *Phys. Rev. B* **96**, 144412 (2017).
23. Barker, J. & Tretiakov, O. A. Static and Dynamical Properties of Antiferromagnetic Skyrmions in the Presence of Applied Current and Temperature. *Phys. Rev. Lett.* **116**, 147203 (2016).
24. Zhang, X. Zhou, Y. & Ezawa, M. Antiferromagnetic Skyrmion: Stability, Creation and Manipulation. *Sci. Rep.* **6**, 24795 (2016).
25. Zhang, X. Zhou, Y. & Ezawa, M. Magnetic bilayer-skyrmions without skyrmion Hall effect. *Nat. Commun.* **7**, 10293 (2016).
26. Zhang, X. et al. Control and manipulation of a magnetic skyrmionium in nanostructures. *Phys. Rev. B* **94**, 094420 (2016).

27. Kolesnikov, A. G. et al. Skyrmionium – high velocity without the skyrmion Hall effect. *Sci. Rep.* **8**, 16966 (2018).
28. Upadhyaya, P. Yu, G. Amiri, P. K. & Wang, K. L. Electric-field guiding of magnetic skyrmions. *Phys. Rev. B* **92**, 134411, (2015).
29. Hirata, Y. et al. Vanishing skyrmion Hall effect at the angular momentum compensation temperature of a ferrimagnet. *Nat. Nanotechnol.*, **14**, 232–236, (2019).
30. Plettenberg, J. Stier, M. & Thorwart, V. Steering of the Skyrmion Hall Angle by Gate Voltages. *Phys. Rev. Lett.* **124**, 207202 (2020)
31. Guo, J.H. Hou, Y. Zhang, X. Pong, Philip W.T. & Zhou, Y. Elimination of the skyrmion Hall effect by tuning perpendicular magnetic anisotropy and spin polarization angle. *Physics Letters A* **456** 128497, (2022).
32. Müller, J et al. Magnetic Skyrmions and Skyrmion Clusters in the Helical Phase of  $\text{Cu}_2\text{OSeO}_3$ . *Phys. Rev. Lett.* **119** , 137201, (2017).
33. Knapman, R. Rodrigues, D. R. Masell, J & Everschor-Sitte, K. Current-induced H-shaped-skyrmion creation and their dynamics in the helical phase. *J. Phys. D: Appl. Phys.* **54**, 404003,(2021).
34. Song, D. et al. Experimental observation of one-dimensional motion of interstitial skyrmion in FeGe. *arXiv:2212.08991 [cond-mat.mes-hall]*.

35. Ezawa, M. Compact merons and skyrmions in thin chiral magnetic films. *Phys. Rev. B* **83**, 100408, (2011)
36. Jena, J. Elliptical Bloch skyrmion chiral twins in an antiskyrmion system. *Nat. Commun* **11**, 1115 (2020).
37. Kumar, V. et al. Detection of antiskyrmions by topological Hall effect in Heusler compounds. *Phys. Rev. B* **101**, 014424 (2020)
38. Ma, T. et al. Tunable Magnetic Antiskyrmion Size and Helical Period from Nanometers to Micrometers in a  $D_{2d}$  Heusler Compound. *Adv. Mater.* **32**, 2002043, (2020).
39. Giri, B. et al. Robust topological Hall effect driven by tunable noncoplanar magnetic state in Mn-Pt-In inverse tetragonal Heusler alloys. *Phys. Rev. B* **102**, 014449, (2020).
40. Lin, S.-Z. Saxena, A. & Batista, C. D. Skyrmion fractionalization and merons in chiral magnets with easy-plane anisotropy. *Phys. Rev. B* **91**, 224407 (2015).
41. Supplementary.
42. Jena, J. et al. Observation of fractional spin textures in a Heusler material. *Nat. Commun.* **13**, 2348 (2022).
43. Tretiakov, O. A. & Tchernyshyov, O. Vortices in thin ferromagnetic films and the skyrmion number. *Phys. Rev. B* **75**, 012408 (2007).
44. Gao, N. et al. Creation and annihilation of topological meron pairs in in-plane magnetized films. *Nat. Commun.* **10**, 5603 (2019).

45. Jani, H. et al. Antiferromagnetic half-skyrmions and bimerons at room temperature. *Nature* **590**, 74–79 (2021).
46. Vousden, M. et al. Skyrmions in thin films with easy-plane magnetocrystalline anisotropy. *Appl. Phys. Lett.* **108**, 132406 (2016).
47. Okumura, S. Hayami, S. Kato, Y. & Motome, Y. Magnetic Hedgehog Lattices in Noncentrosymmetric Metals. *Phys. Rev. B: Condens. Matter Mater. Phys.* **101**, 144416, 2020.
48. Grytsiuk, S. et al. Topological- Chiral Magnetic Interactions Driven by Emergent Orbital Magnetism. *Nat. Commun.* **11**, 511, (2020).
49. Meshcheriakova, O. et al. Large Noncollinearity and Spin Reorientation in the Novel  $\text{Mn}_2\text{RhSn}$  Heusler Magnet. *Phys. Rev. Lett.* **113**, 087203, (2014).
50. Swekis, P. Role of Magnetic Exchange Interactions in Chiral-Type Hall Effects of Epitaxial  $\text{Mn}_x\text{PtSn}$  Films. *ACS Appl. Electron. Mater.* **3**, 3, 1323–1333, (2021).
51. Donahue, M. J. & Porter, D. G. OOMMF Users Guide, Version 1.0, *Interagency Report NISTIR*, (2009).
52. McCray, A. R. et al. Understanding complex magnetic spin textures with simulation-assisted Lorentz transmission electron microscopy. *Phys. Rev. Appl.* **15**, 044025 (2021).
53. Cortés-Ortuño, D. OOMMF Skyrmion Number. *Zenodo doi:10.5281/zenodo.1296536*, (2018).

54. Ishizuka, K. & Allman, B. Phase measurement in electron microscopy using the transport of intensity equation. *J. Electron Microsc.* **54**, 191–197 (2005).

## **Acknowledgments**

A.K.N. acknowledges the Department of Atomic Energy (DAE), the Department of Science and Technology (DST)-Ramanujan research grant (No. SB/S2/RJN-081/2016) and SERB research grant (CRG/2022/002517) of the Government of India for financial support. A.K.N. acknowledges the Max Planck Society for support under the Max Planck-India partner group project. B.G. and A.K.N. acknowledges Dr. A. Das of Solid State Physics Division from Bhabha Atomic Research Center, Mumbai, for providing the neutron diffraction data.

## **Author contributions**

A.K.N. conceived the idea of the present work and led the project. B.G. prepared and characterize polycrystalline samples, prepared the TEM lamellae, carried out the magnetic measurements, and performed the micromagnetic simulations. B.G. and D.C. performed the LTEM measurement. A.D. carried out the neutron diffraction measurements. All authors contribute to the data analysis. B.G., A.K.N., and S.S.P.P. wrote the manuscript.

## **Additional information**

**Competing interests** The authors declare that they have no competing interests.

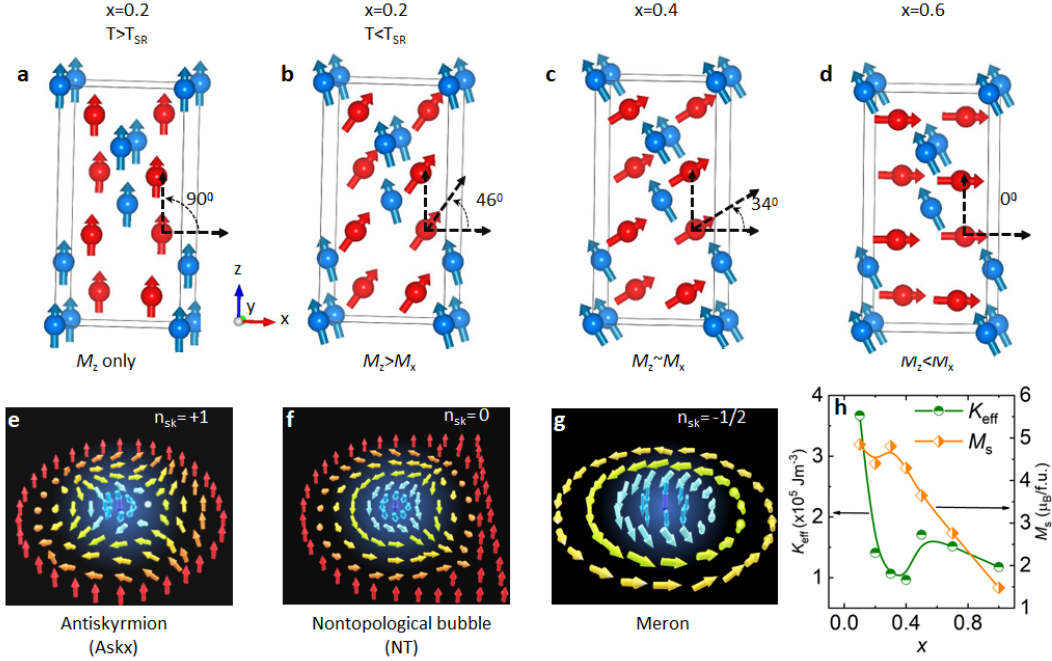


Figure 1: Evolution of magnetic ground states and related spin textures with different In doping in  $\text{Mn}_{1.4}\text{PtSn}_{1-x}\text{In}_x$ . **a** A collinear spin ordering with only out of plane magnetization component  $M_z$ . **b** A noncollinear magnetic ordering with dominant  $M_z$  in comparison to the in plane magnetization  $M_x$ . The magnetic states shown in **a** and **b** correspond to the spin alignment above and below the spin re-orientation transition  $T_{SR}$  for  $x=0.2$ , respectively. **c** A noncollinear spin structure for  $x=0.4$  with comparable  $M_x$  and  $M_z$ . **d** Noncollinear ordering with dominating in-plane magnetic component i.e.,  $M_z < M_x$ . The blue and red balls corresponds to the Mn atoms at 4a and 8d Wyckoff positions, respectively. Evolution of the canting angle of the Mn sublattice at 8d position (red balls) is shown in each figures. All the depicted magnetic ordering are obtained from the powder neutron diffraction experiment. Schematic spin textures of **e** an antiskyrmion, **f** a nontopological bubble (NT), and **g** a meron, generally found for the ground state magnetic ordering shown in figures **a**, **b** and **c**, respectively. The topological charge ( $n_{sk}$ ) for each spin texture is mentioned in the inset of the corresponding figure. **h** Variation of effective anisotropy ( $K_{eff}$ ) with concentration ( $x$ ) and saturation magnetization  $M_S$ .

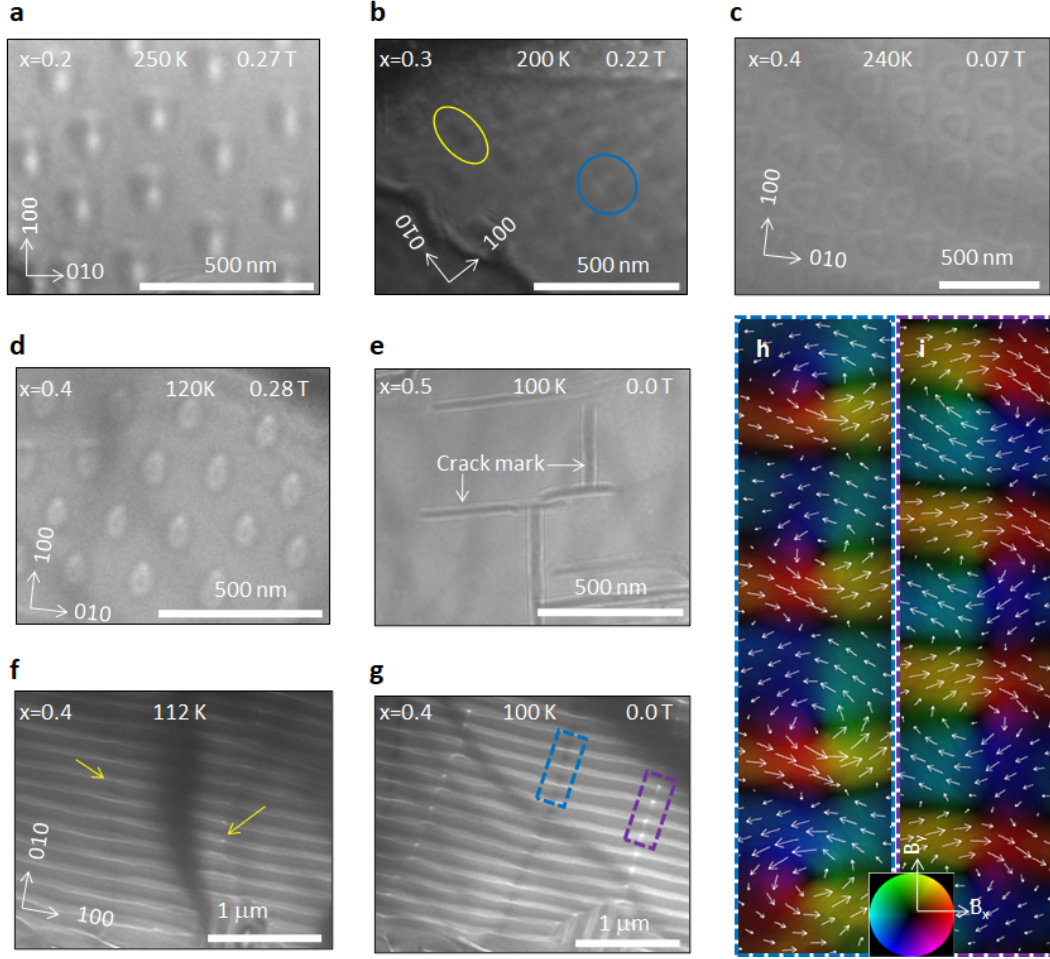


Figure 2: Real space mapping of different spin textures using over focused (OF) Lorentz transmission electron microscopy (LTEM) study of  $\text{Mn}_{1.4}\text{Pt}_{0.9}\text{Pd}_{0.1}\text{Sn}_{1-x}\text{In}_x$  samples for  $x= 0.2$  to  $0.5$ . **a** Evidence of askx lattice in  $x=0.2$  sample at  $T > T_{SR}$ . **b** The coexistence of the askx and skx in  $x=0.3$  sample. The elliptical Bloch skx and askx is marked with the elliptical yellow and blue circles, respectively. **c** Formation of nontopological (NT) bubble phase in  $x = 0.4$ . **d** The coexistence of NT bubbles and elliptical Bloch skx in  $x=0.4$  for at  $T < T_{SR}$ . **e** No LTEM contrast is evident for  $x = 0.5$  sample indicating absence of any spin texture. **f** Appearance of the few (anti)merons as indicated with the yellow arrows for  $x=0.4$ . **g** The Formation of (anti)meron chain within the helical ambiance. **h** and **i** The real space spin texture of the black and white dots contained within the blue and violet dashed rectangle in **g**, respectively. The inset color wheel corresponds to the in-plane magnetic field directions. Fig. **h** and **i** deduced by performing transport of intensity equation (TIE) from the selected region of interest.

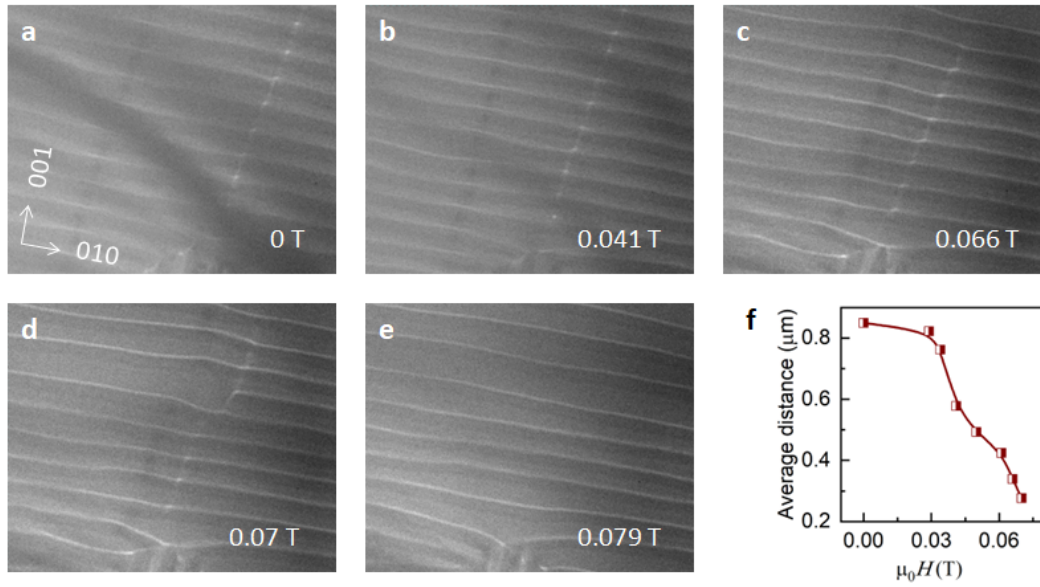


Figure 3: Field evolution of the (anti)meron chains. **a-e** Over-focused images taken at different magnetic fields at  $T = 100$  K for  $x = 0.4$  sample. The width of each figure is  $2 \mu\text{m}$ . **f** Average distance between the meron-antimeron chain with respect to the applied magnetic field. The line is guide to the eye. The average distance is taken by measuring the separation at three different positions: bottom, middle and top region.

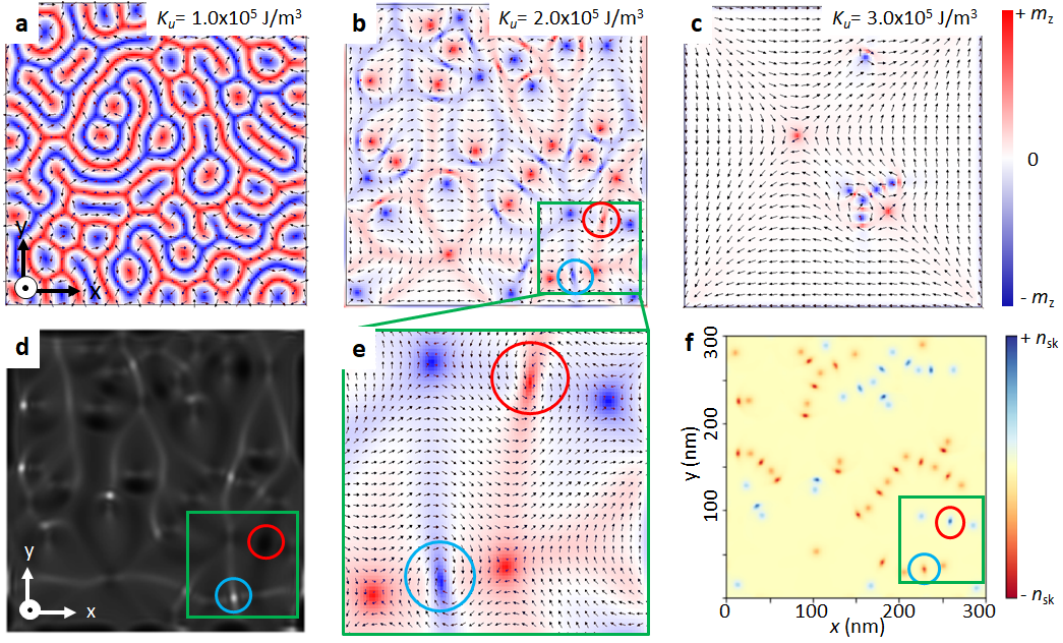


Figure 4: Micromagnetic simulations of (anti)merons. **a-c** Magnetization configuration for different values of in-plane anisotropy constant ( $K_u$ ) obtained from Object Oriented MicroMagnetic Framework (OOMMF) simulation. The color bar represent the  $m_z$  component. **d** The LTEM contrast of the magnetic configuration in **b**. **e** An enlarge view of the chain of meron/antimeron pair enclosed in a green rectangle in **b**. Bloch type merons with core up and down encircled in red and blue color, respectively. **f** Topological charge density (TCD) of **b**. TCD of merons with core up and down is highlighted in **f**. The average magnitude of  $n_{sk} = 0.435$  for each of the (anti)meron in **f**.